Cross-beam pulsed laser fabrication of Free-Standing Nanostructured Carbon Nanotubes-Pt-Ceria Anode with unprecedented electroactivity and durability for ethanol oxidation
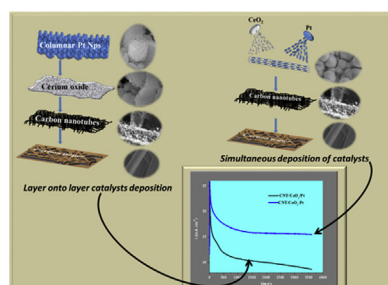
Youling Wang, Amel Tabet-Aoul, Maxime Gougis, Mohamed Mohamedi[*]

Énergie, Matériaux et Télécommunications (EMT), Institut National de la Recherche Scientifique (INRS), Université d'Avant-garde, 1650 Boulevard Lionel Boulet, Varennes, Québec, J3X 1S2, Canada

HIGHLIGHTS

- Free-Standing Nanostructured Carbon Nanotubes-Pt-Ceria Anode.
- Nanostructured Pt-Ceria is prepared by cross-beam pulsed laser deposition.
- The electrode showed excellent electrocatalytic activity and durability to ethanol.

GRAPHICAL ABSTRACT

ARTICLE INFO

ABSTRACT

Owing to its inherent properties such as great capacity to store and release oxygen, lattice oxygen that has a key role in removing the CO poisoning effect, non-toxicity, abundance, low cost and low temperature processing, CeO_2 is emerging as a unique class of electrode material for low temperature polymer electrolyte fuel cells such as direct ethanol fuel cells (DEFCs). However, the maximal exploitation of its functional properties is strictly reliant on the availability of optimized synthesis routes that allow tailor-designing, architecturing and manipulation of CeO_2 in a precise manner when it is combined with other functional materials. Here we use the cross-beam pulsed laser deposition (CBPLD) technique to synthesize free-standing (binderless) $Pt–CeO_2$ nanostructured thin films onto carbon nanotubes as anodes for ethanol oxidation reaction. Further significance of this work is that it establishes the importance in the design of the catalyst layer architecture. Indeed, we demonstrate here that when CeO_2 material is beneath or when it is mixed with Pt, the interactions between Pt with CeO_2 are not similar leading inevitably to different electrocatalytic performances. Given proper tailoring synthesis conditions, CBPLD-developed $Pt–CeO_2$ thin films are remarkably stable and provide electrochemical performance much greater than the layer onto layer CeO_2/Pt architecture.

1. Introduction

Several metal oxides are cheap, abundant and green. Owing to particular native properties and functions of their own, some functional metal oxide (FMO) are emerging as a unique class of electrode materials for a wide spectrum of applications in energy

* Corresponding author. Tel.: +1 514 228 6831; fax: +1 450 929 8102.
E-mail addresses: mybled@yahoo.fr, mohamedi@emt.inrs.ca (M. Mohamedi).

conversion devices such as fuel cells, photoelectrochemical cells [1,2] and energy storage devices, like rechargeable batteries and supercapacitors [3]. Depending on the energy type system, FMO can act as a supporting matrix to improve catalyst dispersion and its stability against sintering and particles aggregation; be itself the electroactive material; or promotes certain electrocatalytic reactions. The future of energy conversion and storage technologies is strictly dependent on the readiness of improved production methods that permit tailor-designing, architecturing and handling of FMOs in a specific way to enhance particular functional properties principally when they are combined with other functional materials.

We have interest in developing FMO-based catalysts for green-based fuel cells principally low temperatures DEFCs. Ethanol is particularly interesting as a green, nontoxic fuel with high theoretical energy density and can be generated from biomass, which could make DEFCs advantageous low greenhouse gas emission power sources. Platinum is found to be the most active catalyst towards electrooxidation of ethanol. However, at Pt catalyst, the complete oxidation of ethanol to CO_2 is not achieved, because of CO poisoning and because the breaking of the C–C bond is not easily achieved at low temperature, which has a detrimental effect on the fuel cell efficiency [4]. It is now clear that a good electrocatalyst must activate C–H, C–O, and C–C bonds where Pt cannot realize these multiple functions alone. Solutions were then sought by combining Pt with one or two additional metals, such as Ru, Re, Rh or Sn among others [5]. These studies revealed somehow an enhancement of ethanol oxidation compared to pure Pt. Nevertheless, the complete oxidation of ethanol to CO_2 at low potentials was not accomplished, instead generating only acetic acid and acetaldehyde.

Cerium dioxide or ceria (CeO_2) is one of the cheapest and most abundant rare earth oxides and represents one of the most actively investigated FMO in materials applications [6–12]. Indeed, its inherent properties such as great capacity to store and release oxygen with little distortion of the lattice [13], as the cerium atom reversibly undergoes oxidation/reduction processes from Ce^{4+} to Ce^{3+}, lattice oxygen that has a key role in removing the CO poisoning effect, non-toxicity and low temperature processing make CeO_2 of great interest for energy conversion systems such as solid oxide fuel cells (SOFC) [14–16], and methanol fuel cells [17].

The chemistry of CeO_2 combined with Pt in ethanol solution is scarce. But the few published studies have shown that CeO_2 can promote the oxidation of ethanol at Pt catalyst [18–23]. Nevertheless, the textural properties of the CeO_2 seem dependent on the processing routes of Pt–CeO_2 composite electrodes often leading to different results. Consequently, several hypotheses have been suggested concerning the function of CeO_2 vis-à-vis the electrooxidation of ethanol. Indeed, CeO_2's role has been argued to be restricted to enhancing Pt nanoparticles dispersion, or to provide oxygen atoms at potentials lower than that achieved by Pt (bifunctional effect), or to modify the electronic structure of Pt and lessens the potential of ethanol adsorption of Pt (the electronic effect); or both the bi-functional and electronic effects. We believe that these discrepancies in interpretation associated to the function of CeO_2 are mainly due to the methods of synthesis of Pt–CeO_2 composites and to the architecturing of the electrode structure itself.

Several methods have been employed to prepare Pt–CeO_2 composites including combined method of impregnation and hot ammonium carbonate precipitation [24]; Pt-doped CeO_2 thin film catalysts prepared by magnetron sputtering [25]; Pt/CeO_2 nanofibers synthesized through an electrospinning method followed by calcination [26]; layer onto layer Pt/CeO_2 prepared by pulsed laser deposition [27]; ultrasound-assisted method to fabricate Pt–CeO_2

hybrids [28]; microwave-assisted polyol process [29]; solution combustion route [30,31]; and wet impregnation method [32].

We report for the first time adapting and optimizing the CBPLD method to synthesize at room temperature Pt–CeO_2 thin films of various surface morphologies onto carbon nanotubes (CNTs). An asymmetric CBPLD geometry makes it possible to mix materials of different targets (here CeO_2 and Pt) directly in the laser plasma with good control over film composition. For further details regarding the general characteristic of CBPLD, the reader is directed towards the review of Tselev et al. [33] Herein, CNTs, which act as the catalyst support are fabricated by chemical vapor deposition (CVD) onto an electrically conductive carbon paper substrate, CP (the current collector, CC), which is the type of gas diffusion layer used in fuel cell devices. Such materials are comprehensively characterized with scanning electron microscopy (SEM), X-ray diffraction (XRD), X-ray photoelectron spectroscopy (XPS), microRaman spectroscopy, and transmission electron microscopy (TEM) techniques and new insights into the interaction of CeO_2 with Pt materials are reported. Afterwards, we study the electroactivity and durability with post-mortem surface morphology of CeO_2–Pt codeposits as well as catalytic promoting properties of CeO_2 to Pt towards the ethanol oxidation reaction (EOR).

A second crucial issue that has not been addressed in the literature concerns the proper way in which CeO_2 must be inserted within the whole catalyst layer in order to fully benefit from its promoting properties in electrocatalysis of fuel cells reactions. There are two ways of including CeO_2 into the catalyst layer, the first one is to intercalate it between the catalyst support and Pt, i.e., the layer onto layer architecture [27]; and the second way is to simultaneously deposit Pt and CeO_2 onto the catalyst support. Now, does CeO_2 have the same effect on the electrocatalytic performance regardless of its position in the catalyst layer? Such question is undertaken here and response is provided that helps a proper architecturing of advanced functional Pt and CeO_2 energy materials.

2. Experimental section

2.1. Materials

Ni (99.99%), Pt (99.99%) and CeO_2 (99.99%) targets used for the PLD and CBLD were purchased from Kurt J. Lesker Co. Untreated carbon paper (CP, Toray) was purchased from Electrochem. The CP is the type of gas diffusion layer used in fuel cell devices (Supplementary data, Fig. S1). Sulfuric acid (H_2SO_4, %) and ethanol (100% purity) were purchased from Agros Organics and Commercial Alcohols inc., respectively. The reactants were used as received without further purification.

2.2. Syntheses

CNTs were grown at 700 °C by CVD using Ni as catalyst deposited by PLD onto CP substrate, acetylene (carbon source), hydrogen and argon (gas carrier) gases at flow rates of 30, 140 and 100 sccm, respectively. Full details regarding the CNTs synthesis can be found elsewhere [34,35].

Pt–CeO_2 composites were prepared by CBPLD (dual beam) by simultaneously depositing Pt and CeO_2. All the deposits were made at room temperature by means of a pulsed KrF excimer laser ($\lambda = 248$ nm, pulse width $= 17$ ns, and repetition rate $= 50$ Hz) using a laser fluence of 4 J cm^{-2}. Pt–CeO_2 composites were deposited under different conditions of background gas pressure in order to obtain different surface morphologies. Prior to each deposition, the chamber was evacuated with a turbo pump (4×10^{-5} Torr). In all cases, the substrate-to-target distance was fixed at 5 cm. In order to obtain a uniform ablation over the target surface, the target was

continuously rotated and translated. Each (Pt–CeO$_2$) catalyst was deposited with 50000 laser pulses giving a Pt loading of 120 μg cm^{-2} (measured by neutron activation analysis, NAA). Three catalysts are considered in this work, namely: (Pt–CeO$_2$)$_{UV}$, (Pt–CeO$_2$)$_{0.5T}$, and (Pt–CeO$_2$)$_{2T}$, where the subscripts UV and T stand for under vaccum and Torr, respectively.

2.3. Material characterization

The surface morphology of the as-prepared samples was characterized using SEM (JEOL, JSM 7401F apparatus) and TEM and high-resolution (HR)-TEM (JEOL-JEM-2100F operating at 200 kV).

The crystalline structure of all samples was determined by XRD using a Bruker D8 Advance diffractometer equipped with a Cu Kα source. The diffractometer was operated at 40 kV and 40 mA. All diffractograms were acquired in the Grazing Incidence Diffraction (GID) scan mode with an incident angle of 2°, 2θ angular step size of 0.05° and acquisition time of 5 s per step.

XPS measurements were performed using a VG Escalab 220i-XL equipped with an Al Kα source (1486.6 eV). The anode was operated at 10 kV and 20 mA. The pass energy of the analyzer was fixed at 20 eV. All samples were analyzed with a spot size of 250 × 1000 μm located approximately in the center of the sample. A survey spectrum ranging from 0 to 1350 eV was first acquired, and then higher resolution multiplex scan spectra (Pt 4f, Ce 3d, O 1s, and C1s core levels) were obtained. Quantification of the elements was carried out with CasaXPS software (Casa Software Ltd.) by fitting the core level spectra after a Shirley background removal. The metallic

components of the Pt 4f region were fitted using a Gaussian/Lorentzian asymmetrically modified line shape, and a Gaussian/Lorentzian line shape was used to fit the other components. The C 1s core level peak at 284.6 eV, resulting from hydrocarbon contaminants at the surface, was used as an internal reference. All spectra have been recalibrated with respect to the C 1s core level peak of adventitious carbon contamination.

2.4. Electrochemical characterization

The electrochemical properties of all samples were evaluated by cyclic voltammetry (CV) and chronoamperometry (CA) in a three compartment electrochemical cell at room temperature. A Pt coil was used as the counter electrode and an Ag/AgCl, 3 M NaCl was used as the reference electrode. The reference electrode was separated from the analyte solution by a Luggin capillary that is very close to the working electrode to minimize the ohmic drop. Data acquisition was conducted with a potentiostat/galvanostat Autolab from EcoChemie. CV measurements were carried out in 0.5 M H$_2$SO$_4$ and in a mixture of 1 M C$_2$H$_5$OH + 0.5 M H$_2$SO$_4$ deaerated solutions. CA was employed for durability evaluation of the catalysts in 1 M C$_2$H$_5$OH + 0.5 M H$_2$SO$_4$. Prior to the electrochemical measurements in ethanol, the surface of the working electrode was cleaned electrochemically by potential cycling in 0.5 M H$_2$SO$_4$. Before each test, dissolved oxygen was removed from the solution by bubbling argon for 30 min. Both the geometric area of the electrode and its Pt loading were used to rationalize the activity of electrocatalyst.
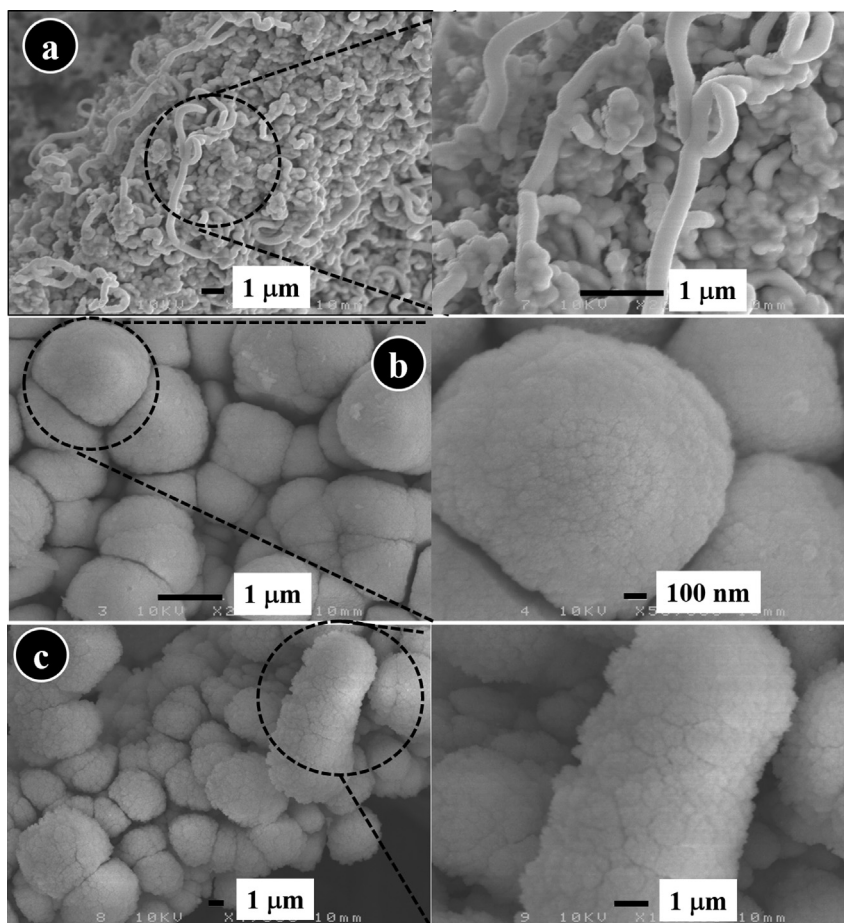

Fig. 1. SEM micrographs with increasing magnification of CBPLD-synthesized (Pt–CeO$_2$) films onto CNTs catalyst support. (a) (Pt–CeO$_2$)$_{UV}$ film; (b) (Pt–CeO$_2$)$_{0.5T}$ film; and (c) (Pt–CeO$_2$)$_{2T}$ film.

3. Results and discussion

3.1. Characterization

Fig. 1 shows SEM images with increasing magnifications of CBPLD synthesized Pt–CeO$_2$ onto CNTs. Considerable differences in the surface morphology are observed between the various deposits. Fig. 1a shows that CNTs are homogeneously coated with a (Pt–CeO$_2$)$_{UV}$ film that is smooth and of closed structure. On the other hand, Pt–CeO$_2$ films deposited under He atmosphere display porous structures. The (Pt–CeO$_2$)$_{0.5T}$ particles gather into highly compacted large grains in a fashion reminiscent of a calotte (Fig. 1b), whereas (Pt–CeO$_2$)$_{2T}$ particles assemble into cauliflower or broccoli-like arrangements (Fig. 1c). SEM images at higher magnification shows that the surface topography of (Pt–CeO$_2$)$_{2T}$ is more porous but looks scaly and brittle.

The XRD profiles of the (Pt–CeO$_2$) samples show the presence of diffraction peaks (111), (200), (220), and (311) corresponding to the fcc fluorite structure of CeO$_2$ (JCPDS file 13-1002) (Fig. S2). The Pt(111) reflection was observed at the (Pt–CeO$_2$)$_{UV}$ but no detectable Pt at the (Pt–CeO$_2$)$_{0.5T}$ and (Pt–CeO$_2$)$_{2T}$ samples. However, the existence of Pt particles was verified by using energy dispersion spectroscopy (EDS) under transmission electron microscope (Fig. S3).

The PLD involves complex physical processes of laser–material interaction during the impact of the high-power pulsed radiation on a solid target [36,37]. Briefly, the morphological differences observed between the deposited Pt–CeO$_2$ films are principally due to the decrease of the kinetic energy of the deposited species which varies with the atmosphere in the deposition chamber. The variation of the kinetic energy of the plasma species induces a modification of the surface mobility of the deposited species. In vacuum, the absence of collisions between the expanding plasma and the surrounding gas molecules leads to a situation where the kinetic energy of the plasma species is the highest. Greater surface mobility of the deposited species transforms into denser films and surface reorganization that lead to minimization of the energy, which is the case observed here for (Pt–CeO)$_{UV}$ (Fig. 1a). On the contrary, the presence of an atmosphere in the deposition chamber will decrease the kinetic energy of the plasma species. Owing to that fact, the expanding plasma will interact more strongly with the molecules of the gas. As the pressure in the deposition chamber is increased, the likelihood for the plasma species to lose part of their kinetic energy through a contact (collision) with the gas molecules will be also increased, thus lowering the kinetic energy of the plasma species. This decrease of the kinetic energy of the plasma species induces a modification of the surface mobility of the
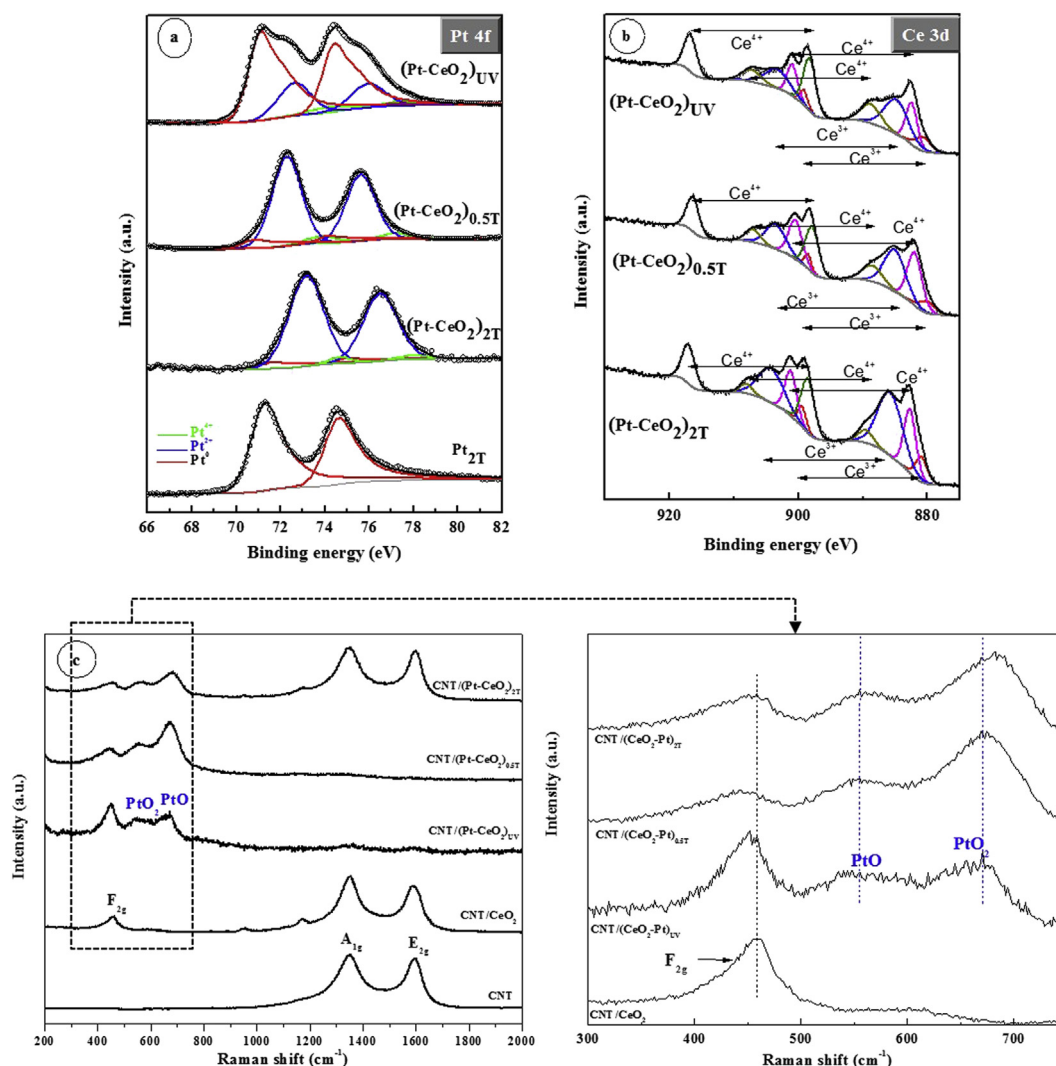

Fig. 2. Spectroscopy analyses of CBPLD-synthesized (Pt–CeO$_2$) films. High-resolution XPS spectra of (a) Pt 4f core level (the spectrum of pure Pt is shown for referencing) and (b) Ce 3d core level. (c) Raman spectra. The Raman spectra of bare CNTs and CNT/CeO$_2$ materials are shown for referencing.

Table 1
XPS parameters extracted from Fig. 2a and b.

Sample	Pt^0		Pt^{2+}		Pt^{4+}		Pt^{2+}/Pt^{4+}	Ce^{3+}/Ce^{4+}
	BE (eV)	at%	BE (eV)	at%	BE (eV)	at%		
Pt	71.30	100	—	—	—	—	—	—
$(Pt–CeO_2)_{UV}$	71.12	62.97	72.63	31.45	74.12	5.58	5.64	0.64
$(Pt–CeO_2)_{0.5T}$	70.84	6.32	72.30	85.96	73.84	7.03	12.23	0.61
$(Pt–CeO_2)_{2T}$	71.67	4.71	73.17	91.06	74.67	4.23	21.52	1.02

deposited species leading to a porous film (Fig. 1b and c). More details regarding the influence of the atmosphere chamber on the physical processes of laser–material interaction can be found elsewhere [33,36–38].

The high-resolution Pt 4f and Ce 3d core level XPS spectra of the CNT/(Pt–CeO$_2$) thin films are shown in Fig. 2a and Fig. 2b, respectively. For referencing, the Pt 4f core level spectrum of pure PLD-deposited Pt onto CNTs is also reported in Fig. 2a. The Pt 4f spectrum of pure Pt shows a doublet containing a low energy band (Pt $4f_{7/2}$) and a high energy band (Pt $4f_{5/2}$) at 71.30 and 74.58 eV, respectively. The 3.28 eV binding energy (BE) difference between the Pt $4f_{7/2}$ and Pt $4f_{5/2}$ is consistent with Pt being in a metallic state [39]. No other chemical states of Pt were identified and satisfactory fitting of each core level peak was obtained using only one component with an asymmetric profile. On the other hand, the XPS spectra of the co-deposited CNT/(Pt–CeO$_2$) films reveal that Pt is present in more than one oxidation states. To identify the different chemical states of Pt, the spectra could be fitted by three overlapping curves, labeled Pt^0, Pt^{2+}, and Pt^{4+}. Pt–CeO$_2$ composite exhibiting ionized platinum have been observed by some researchers [25,40,41], and this is the first time it is observed for (Pt–CeO$_2$) films prepared by CBPLD technique. The position and relative amount of Pt species were estimated from the relative intensities of these three peaks, and the results are summarized in Table 1. The position of Pt^{2+} and Pt^{4+} are in accordance with these reported in the literature [42–44]. From Table 1, it can be noted that (Pt–CeO$_2$)$_{UV}$ contains significant amount of Pt^0 of 63 at%. The amount of Pt^0 significantly decreased to less than 7 at% for samples deposited under He atmosphere. Furthermore, the Pt^{2+}/Pt^{4+} ratio increased with the increase of the background pressure. The Ce 3d core level XPS spectra of the (Pt–CeO$_2$) films reported in Fig. 2b consist of three $3d_{5/2}$–$3d_{3/2}$ doublets characteristic of Ce^{4+} (CeO$_2$) and two doublets of Ce^{3+} [45,46]. Table 1 shows the Ce^{3+}/Ce^{4+} ratio obtained by calculating sums of areas of the Ce 3d doublets. The (Pt–CeO$_2$)$_{2T}$ displayed the highest Ce^{3+}/Ce^{4+} ratio, while (Pt–CeO$_2$)$_{0.5T}$ and (Pt–CeO$_2$)$_{UV}$ showed ratios close to each other.

The results of Fig. 2a and b show that CeO$_2$ was reduced during its simultaneous deposition with Pt. These observations are similar to Pt doped CeO$_2$ layers deposited by (rf) magnetron sputtering on CNTs [41,47,48]. The authors assumed this behavior to a relative increase of oxygen vacancies, which are present at the cerium oxide crystallite surface. They supposed that Pt^{4+} (PtO$_2$) species correspond to Pt cations substituting Ce cations in the CeO$_2$ lattice, and that Pt^{2+} are formed by Pt atoms located at the crystallite surface. The authors further observed an increase in the Pt^{2+}/Pt^{4+} ratio with Pt content which could be hypothetically explained by higher segregation of platinum to the grain boundary region with increasing dose of Pt doping. Despite that in our work, the amount of Pt was the same for all the (Pt–CeO$_2$) samples, we do however observe an increase in the Pt^{2+}/Pt^{4+} with the increase of the background pressure (Table 1). Such trend is observed for the first time and will be a subject of study in the future.

The Raman spectra of the pristine CNTs, CNT/CeO$_2$, and CNT/(Pt–CeO$_2$) samples are presented in Fig. 2c. The spectrum of pristine CNTs exhibits two main characteristic bands, the first order G

mode (E$_{2g}$ symmetry) at ~1596 cm^{-1} ascribed to a regular sp^2 graphitic network, and the D mode (A$_{1g}$ symmetry) at ~1348 cm^{-1}, which reflects the disorder and defects in the carbon lattice [49]. In addition to the D and G bands characteristics of the CNTs, the spectrum of the CNT/CeO$_2$ layers displays bands within 200~1170 cm^{-1} range. The band located at ~458.5 cm^{-1} is ascribed to triply degenerate Raman active F$_{2g}$ mode [50]. Only the oxygen atoms move in this mode, which is therefore very sensitive to the oxygen sublattice disorder resulting from processing and/or grain-size-induced non-stoichiometry.

Mixing Pt to ceria definitely produces a dramatic change in the Raman response and clearly reflects interactions between CeO$_2$ and Pt. The position of the F$_{2g}$ band and its corresponding full width half maximum (FWHM) for all the samples are resumed in Table 2. For a bulk CeO$_2$, the F$_{2g}$ mode is located at ~465.4 cm^{-1} with an FWHM of 9.5 cm^{-1} [51,52]. As can be seen from Table 2, all CeO$_2$-based samples synthesized under our conditions displayed a red shift and broadening of the FWHM compared to bulk CeO$_2$. Some authors have reported red shift and broadening of the phonons in ceria materials, which was differently interpreted. It was ascribed for example to the formation of nanocrystalline phase for the film [53], or to poorer crystalline quality for the film, or to the softening of the Raman F$_{2g}$ mode in nanocrystalline ceria (457 cm^{-1} versus 464.3 cm^{-1} in polycrystalline sample) as a consequence of phonon confinement effects [54]. Other researchers simultaneously considered phonon confinement, stress, size distribution and non-stoichiometry as possible causes for grain size induced variations of ceria Raman spectra [50]. The Raman line broadening of CeO$_2$ has been described by the dependence of the half-width, Γ, on the inverse of grain size, d_g, which follows a linear behavior [55–57].

$$\Gamma\left(cm^{-1}\right) = 10 + (124.7/d_g) \qquad (1)$$

As can be seen from Table 2, the Raman line broadens with decreasing grain size. Using the above relation, we found the crystal size of the CeO$_2$ in the (Pt–CeO$_2$) samples to be 4.8, 3.6, and 2.4 nm for the (Pt–CeO$_2$)$_{UV}$, (Pt–CeO$_2$)$_{0.5T}$ and (Pt–CeO$_2$)$_{2T}$, respectively (Table 2). Fig. S4 shows that these data follow a linear behavior, which is in good correlation with that reported for nanocrystalline CeO$_2$ powder specimens [51].

In addition to the F$_{2g}$ mode, the three CNT/(Pt–CeO$_2$) samples showed two new Raman bands at ~547.3 and ~678.3 cm^{-1} (Fig. 2c). The 678.3 cm^{-1} vibration is consistent with the vibration of crystalline PtO, whereas the 547.3 cm^{-1} vibration is consistent with the vibration of crystalline PtO$_2$ [58,59]. In Fig. 2c is also reported the

Table 2
Raman parameters of CeO$_2$ extracted from Fig. 2c.

Sample	F_{2g} (cm^{-1})	FWHM (cm^{-1})	Grain size nm
CNT/CeO$_2$	458.5	45.0	3.6
CNT/(Pt–CeO$_2$)$_{UV}$	452.6	35.8	4.8
CNT/(Pt–CeO$_2$)$_{0.5T}$	446.0	44.5	3.6
CNT/(Pt–CeO$_2$)$_{2T}$	456.4	61.5	2.4

Raman spectrum of CNT/CeO$_2$/Pt layer onto layer architecture, which does not show the presence of Pt-oxide. The results from Raman are a clear demonstration of oxidation of Pt in the co-deposited samples. Consequently, it can be concluded that the Pt^{4+} (PtO$_2$ species) appearing in the XPS correspond to Pt^{4+} substituting Ce^{4+} cations in the CeO$_2$ lattice, which corroborates the assumption of Fiala et al. [47].

Fig. 3 shows TEM and HR-TEM images of the different CBPLD-synthesized (Pt–CeO$_2$) films onto CNTs. In all cases, it can be seen that CNTs are well-coated with Pt–CeO$_2$ films. In addition, the images confirm the marked difference in the morphology of the different deposits, i.e., a highly closed structure of the (Pt–CeO$_2$)$_{UV}$ film and the porous structure for the (Pt–CeO$_2$)$_{0.5T}$ and (Pt–CeO$_2$)$_{2T}$ films. The crystallographic orientation by means of selected area electron diffraction (SAED) patterns of the CNT/(Pt–CeO$_2$)$_{UV}$ film reveal both the presence of polycrystalline Pt and CeO$_2$ (Fig. S5a). On the other hand, the SAED patterns of both CNT/(Pt–CeO$_2$)$_{0.5T}$ (Fig. S5b) and CNT/(Pt–CeO$_2$)$_{2T}$ (Fig. S5c) show the presence of CeO$_2$, Ce$_2$O$_3$ and PtO but no Pt. These observations are in line with those obtained with XRD, XPS and Raman analyses.

3.2. Electroactivity

Fig. 4a presents CVs with potential scan rate of 50 mV s^{-1} at the CNT/(Pt–CeO$_2$) electrodes in 0.5 M H$_2$SO$_4$ deaerated solution. The CVs include the very well-known hydrogen adsorption (H$_{ads}$) and desorption (H$_{des}$) peaks in the potential region of ca. −0.2 to 0.1 V vs. Ag/AgCl [60,61]. The Pt oxide formation occurs within 0.50~0.6 V range where as its counterpart reduction peak potential takes place between 0.50 and 0.55 V vs. Ag/AgCl (as depicted in Fig. 4a). Although similar electrochemical features are observed but their resolution depended markedly on the morphology of the different (Pt–CeO$_2$) samples. First, the characteristic peaks in the H$_{ads}$/H$_{des}$ region at (Pt–CeO$_2$)$_{0.5T}$ sample are distinctively sharper, which clearly indicates the higher number and better cleanliness of the exposed Pt surfaces in the (Pt–CeO$_2$)$_{0.5T}$ sample [62]. Second, the greater symmetric peak shapes in the H$_{ads}$/H$_{des}$ region of (Pt–CeO$_2$)$_{0.5T}$ sample are also suggestive of a highly reversible hydrogen adsorption/desorption process as compared with that of (Pt–CeO$_2$)$_{UV}$ and (Pt–CeO$_2$)$_{2T}$ samples [63]. Finally, the CV profile of (Pt–CeO$_2$)$_{0.5T}$ sample displays a higher capacitive current after the Pt oxide formation, which indicates that this material possesses higher surface area.

In addition, from Fig. 4a, it is seen that the voltammetric current responses of the samples in the H$_{ads}$/H$_{des}$ region are different. Since the Pt loading in all the samples is the same, the variation in the current response is attributed to the difference in the number of electroactive sites in the samples for hydrogen adsorption/desorption. Basically, this is characterized as the real electroactive

surface area (*ESA*) of the samples, which can be determined as follows:

$$ESA = Q_H/Q_{ref} \qquad (2)$$

Q_H is obtained by integrating the charge in the hydrogen adsorption region of the CVs shown in Fig. 4a, corrected for the double-layer current by back extrapolation of the current from the double layer region. Q_{ref} is a conversion factor of 210 μC cm^{-2}, generally accepted for polycrystalline Pt electrodes [64]. The *ESA* of Pt nanocrystals in (Pt–CeO$_2$)$_{UV}$, (Pt–CeO$_2$)$_{0.5T}$, and (Pt–CeO$_2$)$_{2T}$ samples was estimated to be 5.61, 16.80, and 2.77 cm^2 respectively. The electrochemical activity of the Pt–CeO$_2$ catalysts can be further assessed with the area specific activity (*ASA*) (normalized by the Pt catalyst loading to generate mass activity) as follows:

$$ASA = Q_H/(Q_{ref} \times Pt\ loading \times A_g) \qquad (3)$$

where A_g represents the geometric electrode area.

Note that the *ESA* provides an intrinsic electrocatalytic value of a catalyst, whereas *ASA* is an essential parameter concerning the practical application, i.e., the economic value of the catalyst, which basically is the activity normalized to cost. The *ASA* of Pt in (Pt–CeO$_2$)$_{UV}$, (Pt–CeO$_2$)$_{0.5T}$, and (Pt–CeO$_2$)$_{2T}$ samples was estimated to be 8.81, 38.2, and 6.46 m^2 g^{-1}, respectively. These results show that, despite of similar Pt loading in each sample, the (Pt–CeO$_2$)$_{0.5T}$ electrode displayed much higher *ESA* and *ASA* values.

Afterwards, the electrocatalytic activity of the Pt–CeO$_2$ samples was investigated towards ethanol electrooxidation. Fig. 4b shows linear scan voltammograms (LSVs) recorded in 0.5 M H$_2$SO$_4$+ 1 M C$_2$H$_5$OH solution with slow scan rate of 5 mV s^{-1} (quasi-steady state). The LSVs at all the electrodes displayed well defined characteristic ethanol oxidation waves in agreement with the literature [65,66]. The insert of Fig. 4b shows that (Pt–CeO$_2$)$_{0.5T}$ catalyst oxidizes ethanol at potentials lower than those delivered by (Pt–CeO$_2$)$_{UV}$ and (Pt–CeO$_2$)$_{2T}$ electrodes. Fig. 5c compares peak current densities, i_p (mA cm^{-2}), and the specific mass activity, *SMA* (peak current divided by the Pt loading) extracted from LSVs of Fig. 4b. It can be observed that (Pt–CeO$_2$)$_{0.5T}$ electrode displayed the highest i_p and *SMA* of 35.10 mA cm^{-2} and 292.5 mA mg$_{Pt}^{-1}$, respectively. Such values are particularly significant since they are obtained at scan rates as low as 5 mV s^{-1}.

3.3. Durability

From a practical point of view, the durability of a catalyst during long-time operation is crucial. Long-term chronoamperometry tests were carried out by stepping the potential from the open circuit potential to 0.6 vs Ag/AgCl in 0.5 M H$_2$SO$_4$ + 1 M C$_2$H$_5$OH.
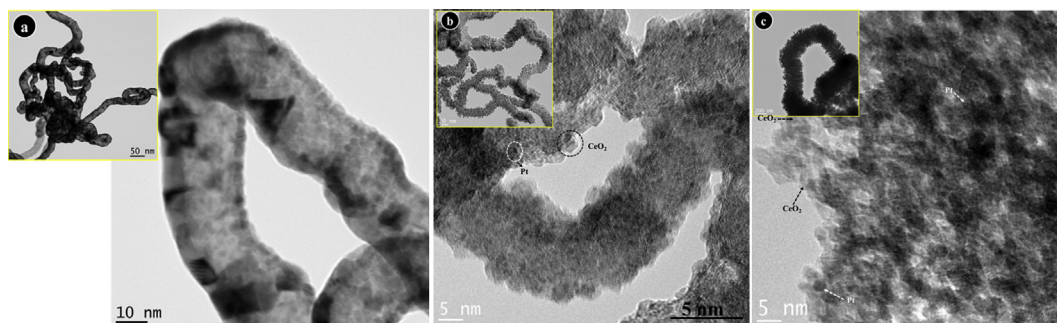

Fig. 3. Upper left panels are TEM and main panels are HR-TEM micrographs of CBPLD-synthesized (Pt–CeO$_2$) films onto CNTs catalyst support. (a) (Pt–CeO$_2$)$_{UV}$ film; (b) (Pt–CeO$_2$)$_{0.5T}$ film; and (c) (Pt–CeO$_2$)$_{2T}$ film.
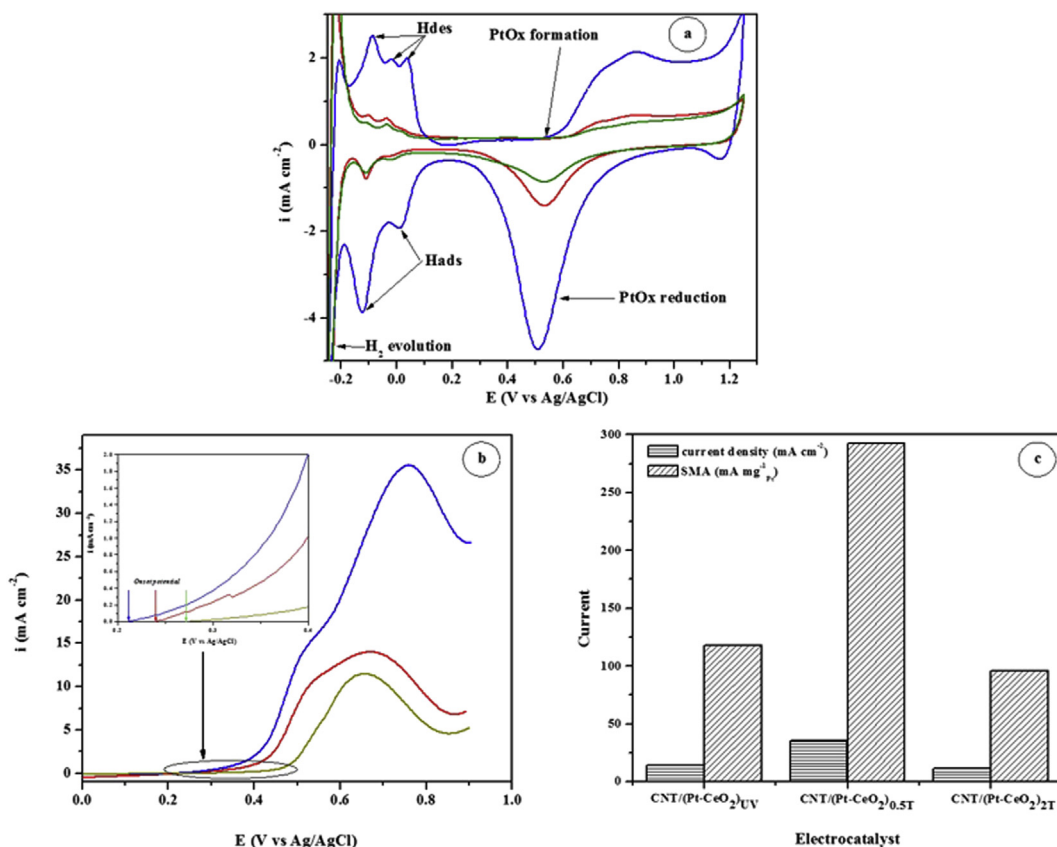
Fig. 4. Electroactivity of CBPLD-synthesized (Pt—CeO₂) films onto CNTs catalyst support. (a) Cyclic voltammetry in 0.5 M H₂SO₄-argon purged solution with a potential scan rate of 50 mV s⁻¹. (b) Linear scan voltammetry in 0.5 M H₂SO₄ + 1 M C₂H₅OH argon purged solution with a potential scan rate of 5 mV s⁻¹. (c) Current peak density and *SMA* values extracted from Fig. 4b. (Pt—CeO₂)$_{UV}$ (red line), (Pt—CeO₂)$_{0.5T}$ (blue line) and (Pt—CeO₂)$_{2T}$ (green line). (For interpretation of the references to color in this figure legend, the reader is referred to the web version of this article.)
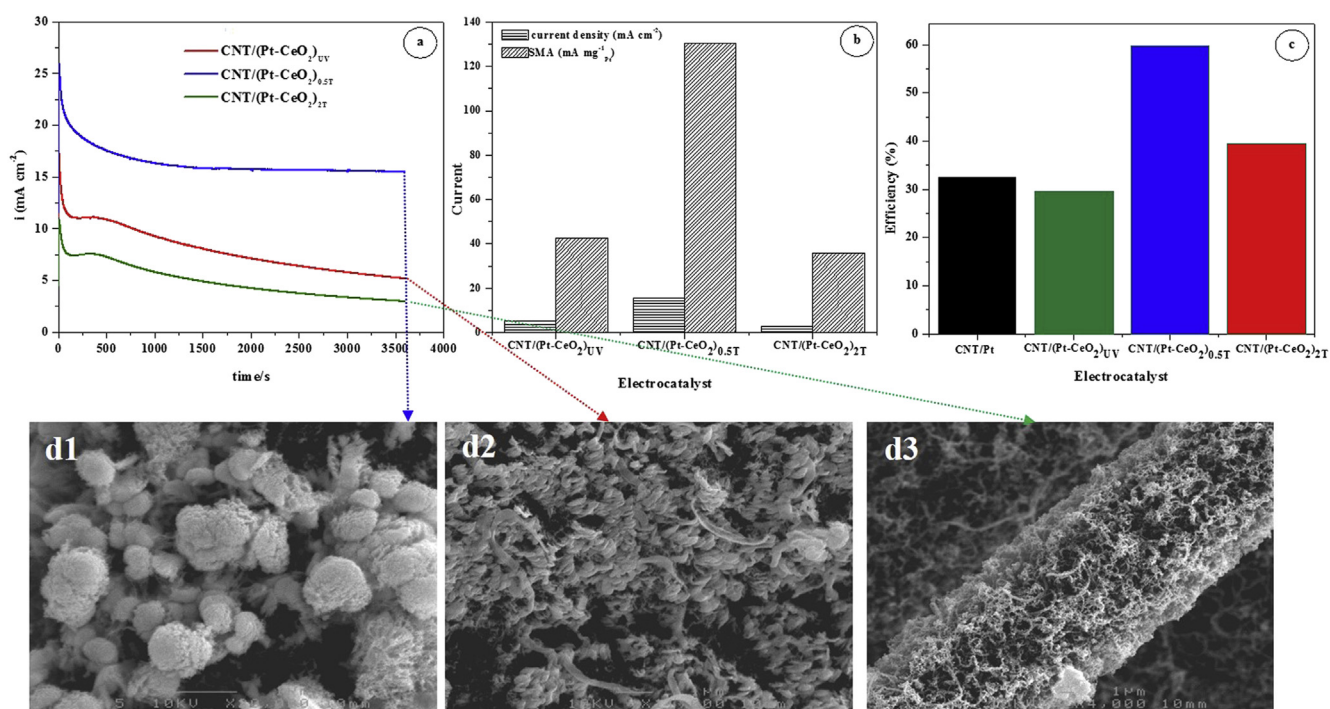

Fig. 5. (a) Durability in 0.5 M H₂SO₄ + 1 M C₂H₅OH argon purged solution of CBPLD-synthesized (Pt—CeO₂) films onto CNTs catalyst support. (b) Steady-state density and *SMA* values extracted from Fig. 5a. (c) Efficiency (the efficiency of CNT/Pt catalyst is shown for referencing). Bottom are SEM images taken after durability measurements shown in Fig. 5a.

The current values were recorded for 1 h, and the resulting current density-time (*i-t*) curves are shown in Fig. 5a. All *i-t* responses displayed an initial fast decay due to the rapid increase of the surface coverage by intermediate species, such as adsorbed CO during ethanol oxidation reaction. However, there is a marked difference in the durability between the three (Pt–CeO$_2$) catalysts. The current continued to decrease slowly at the (Pt–CeO$_2$)$_{UV}$ and (Pt–CeO$_2$)$_{2T}$ catalysts until reaching a quasi-steady state upon 1 h operation. On the other hand, the current rapidly attained a perfectly steady-state at the (Pt–CeO$_2$)$_{0.5T}$ catalyst. Fig. 5b resumes the steady-state current densities (*i*$_{ss}$) altogether with the *SMA* (steady-state current divided by the Pt loading) which shows that (Pt–CeO$_2$)$_{0.5T}$ catalyst delivered a large *SMA* of 130 mA mg$_{Pt}^{-1}$ three times greater than (Pt–CeO$_2$)$_{UV}$ and (Pt–CeO$_2$)$_{2T}$ electrodes.

The durability can be further quantified by plotting the stability efficiency calculated as *i*$_{ss}$ from Fig. 5a divided by the initial current density (*t* = 0). Fig. 5c, confirms that the (Pt–CeO$_2$)$_{0.5T}$ electrode outperforms the other electrodes by retaining about 60% of its initial activity demonstrating by that a high tolerance to CO poisoning.

Post-mortem analysis by SEM of the surface morphology after durability measurements are shown in Fig. 5d1–d3. The CNT/(Pt–CeO$_2$)$_{UV}$ surface became flaky which is in fact the Pt–CeO$_2$ catalyst that has detached from the beneath CNTs (Fig. 5d2). Worse was the stability of the (Pt–CeO$_2$)$_{2T}$ catalyst, which has completely disconnected from the CNTs (Fig. 5d3) and has fallen in the electrolyte. On the other hand, the (Pt–CeO$_2$)$_{0.5T}$ catalyst (Fig. 5d1) has not undergone any major change The obtained *ESA*, *ASA* and results of Figs. 4 and 5 indicate that the electrochemical performance is not significantly different between the (Pt–CeO$_2$)$_{UV}$ and the (Pt–CeO$_2$)$_{2T}$ electrodes. Nevertheless, the (Pt–CeO$_2$)$_{0.5T}$ far exceeds the latter two in terms of electroactivity and durability.

The formation of ionized species Pt$^{2+,4+}$ has been observed for Pt-doped cerium oxide films prepared by rf sputtering on a Si wafer, and on multiwall carbon nanotubes (MWCNTs) [48]. The Pt^{2+}/Pt^{4+} ratio depended on the deposition angle and increased in the case of the film deposition on the MWCNTs. Besides the effect of the substrate, the authors further observed an increase of Pt^{2+}/Pt^{4+} ratio with Pt content onto MWCNTs substrate, which was explained by higher segregation of platinum to the CeO$_2$ grain boundary region. When used as an anode material in hydrogen-fed polymer membrane fuel cell (PMFC), Pt–CeO$_2$ films deposited on carbon nanotubes (CNTs) exhibits very high specific power [41]. The activity of this material is explained by high activity of embedded Pt$^{2+,4+}$ cations toward H$_2$ dissociation and formation of protonic hydrogen.

In our work with the CBPLD technique, the substrate (CNTs), the Pt loading, the laser fluence, and the substrate-to-target distance were fixed. It was only the background atmosphere that was changed and we do however observe an increase of the Pt^{2+}/Pt^{4+} ratio with the background gas pressure (Table 1). Such phenomenon is observed for the first time with CBPLD method and is very complex to explain for the time being.

Nevertheless, in our work, the electrochemical performance cannot be connected to the presence of high concentration of Pt^{2+} since the (Pt–CeO$_2$)$_{2T}$ showed the least electroactivity. For instance, we can only link the electrochemical performance to the morphology of the (Pt–CeO$_2$) deposits. The (Pt–CeO$_2$)$_{UV}$ film is of closed structure (Figs. 1 and 3a), which is not suitable for a better accessibility of the electrolyte. The morphology of the (Pt–CeO$_2$)$_{UV}$ looks porous but mechanically fragile (Figs. 1 and 3c). On the other
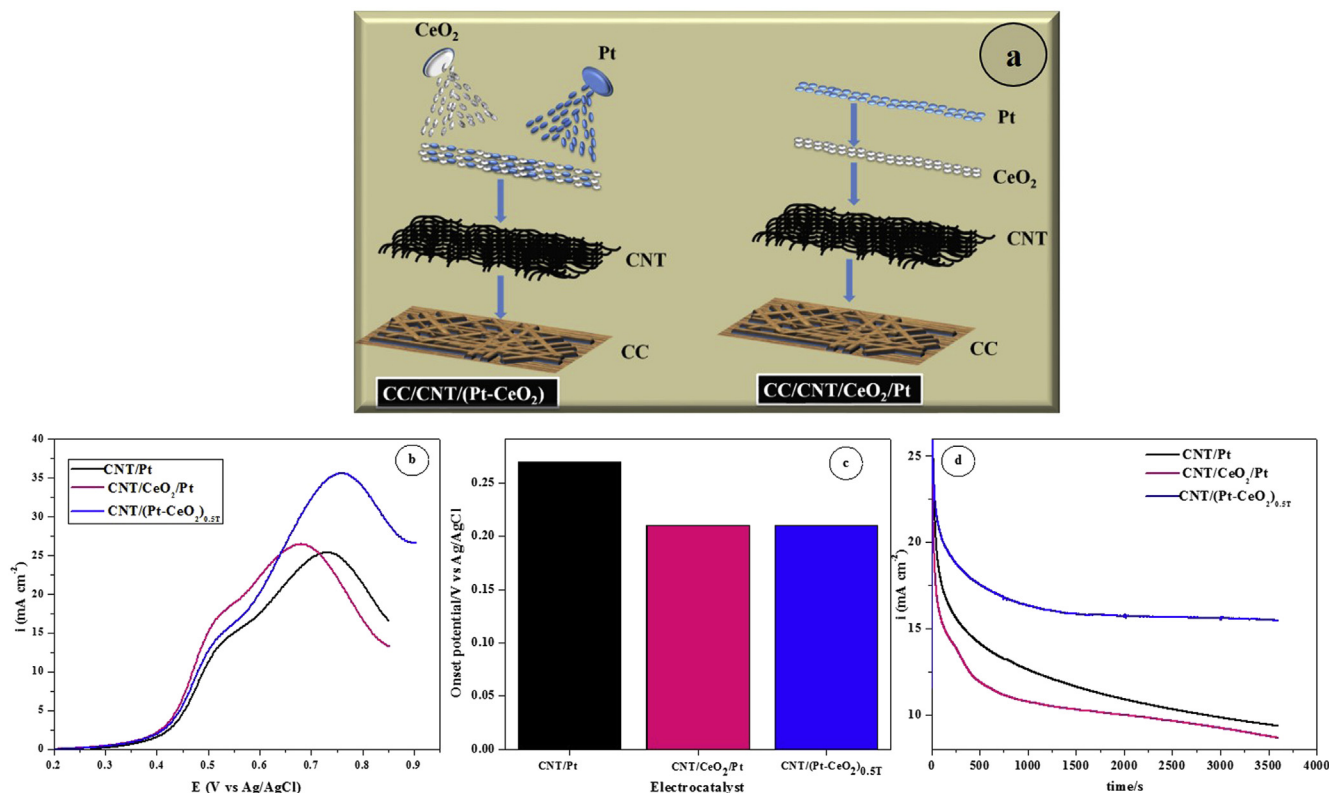

Fig. 6. (a) Rough representation of two catalyst layer architectures in which CeO$_2$ is positioned differently: (left) mixed (Pt–CeO$_2$) onto CNTs vs (right) layer onto layer (CNT/CeO$_2$/Pt). (b) Linear scan voltammetry in 0.5 M H$_2$SO$_4$ + 1 M C$_2$H$_5$OH argon-purged solution with a potential scan rate of 5 mV s^{-1}. (c) Onset potential of ethanol oxidation reaction. (d) Durability in 0.5 M H$_2$SO$_4$ + 1 M C$_2$H$_5$OH argon purged solution. The results of CNT/Pt catalyst layer are shown for referencing.

hand, the $(Pt-CeO_2)_{0.5T}$ particles arrangement into uniform and compact calottes-like shapes (Fig. 1b) with higher *ESA* and surface roughness factor (*ESA* divided by the geometric area of the electrode) of about 46 compared to around 11 for $(Pt-CeO_2)_{UV}$ and $(Pt-CeO_2)_{2T}$ electrodes, explain the high electrochemical performance and durability of the $(Pt-CeO_2)_{0.5T}$ anode catalyst. This is due to the highly dispersed Pt crystallites, which expose a larger number of active sites for surface reactions. This is evident from the hydrogen adsorption/desorption during CV measurements (Fig. 4a), which shows a higher *ESA* of Pt crystallites dispersed on the $(Pt-CeO_2)_{0.5T}$ sample as compared with $(Pt-CeO_2)_{UV}$ and $(Pt-CeO_2)_{2T}$ samples.

3.4. The catalyst layer architecture: co-deposited Pt–CeO₂ versus layer onto layer deposited CeO₂/Pt

As mentioned at the end of the introduction part, we will address here the approach on whether or not CeO_2 adds the same functionality to the Pt catalyst when it is arranged differently in the catalytic layer. Fig. 6a shows a rough representation of two architectures of the catalyst layer in which CeO_2 is incorporated differently. The first architecture is the one developed in this work that is $CC/CNT/(Pt-CeO_2)$, whereas in the second one, CeO_2 is intercalated between CNTs and Pt $(CC/CNT/CeO_2/Pt)$. In the $CC/CNT/CeO_2/Pt$ architecture, CeO_2 and Pt were also deposited by PLD and we have already reported their synthesis, characterization and electro-activity towards ethanol electrooxidation [27]. XPS analysis of the $CC/CNT/CeO_2/Pt$ structures did not show a change in the electronic structure of Pt deposited onto the CeO_2 layer. The only effect observed from the interaction between CeO_2 and Pt was the reduction in the particle size of Pt by CeO_2 [27].

Fig. 6b compares LSVs at $CC/CNT/Pt$, $CC/CNT/CeO_2/Pt$ and $CC/CNT/(Pt-CeO_2)_{0.5T}$ electrodes in ethanol containing solution. The onset potential for ethanol electrooxidation reaction is of 0.27 V vs Ag/AgCl at $CC/CNT/Pt$ electrode, whereas at both $CC/CNT/CeO_2/Pt$ and $CNT/(CeO_2-Pt)_{0.5T}$ is 0.20 V vs Ag/AgCl (Fig. 6c). On the other hand, a marked difference is observed in the current peak densities delivered by the electrodes. The LSVs show that the current peak density at the $CC/CNT/(Pt-CeO_2)_{0.5T}$ electrode is 35.65 mA cm^{-2} vs 26.45 mA cm^{-2} at the $CC/CNT/CeO_2/Pt$ electrode. The durability performance of the $CC/CNT/CeO_2/Pt$-architecture is very bad as can be seen in Fig. 6d, the current declined rapidly and approached zero upon 1 h of testing, which indicates bad tolerance to CO-poisoning.

In light of these observations, we can argue that CeO_2 brings a beneficial effect to Pt vis-à-vis the electrooxidation of ethanol. However the extent of such favorable influence clearly depends on the position of CeO_2 within the whole catalyst layer. When intercalated between the catalyst support (CNTs in this case) and the Pt catalyst, CeO_2 is prone to adsorption of OH species at potentials lower than those achieved by pure Pt. However with such catalyst layer structure, the number of OH_{ads} is not sufficient for removal of adjacent CO_{ads} on Pt as observed with durability results (Fig. 6d, pink line). On the other hand, CeO_2 when deposited simultaneously with Pt modifies the electronic structure of Pt (electronic effect) and is prone to adsorption of higher number of OH adsorbed species at lower potentials (bi-functional effect) [67,68], which provides significant CO-poisoning tolerance to Pt during the ethanol electrooxidation reaction and by that high durability (Fig. 6d, blue line). However, in addition to the electronic effect and bi-functional effect, the surface morphology is another decisive parameter. Indeed, within the three co-deposited $(Pt-CeO_2)$ samples, the unique morphology of the $(Pt-CeO_2)_{0.5T}$ sample (Fig. 1b) seems to offer a more pronounced oxygen mobility of OH_{ads} on the surface of the CeO_2. This, in effect boosts the conversion of adsorbed CO to free CO_2 on the $(Pt-CeO_2)_{0.5T}$ sample.

4. Conclusions

The CBPLD technique is employed and optimized for the first time to simultaneously deposit nanostructured thin films of $Pt-CeO_2$ catalysts onto CNTs directly grown on anode gas diffusion layer that is employed for the fuel cell catalyst fabrication. The thin film microstructure was investigated as function of CBPLD deposition parameters such as the ambient gas pressure giving rise to different microstructures with different electrocatalytic properties.

From SEM, TEM, XRD, XPS and Raman analyses, it was observed that the extent of the interaction between Pt and CeO_2 was influenced by the PLD-background gas pressure condition during deposition. The films deposited under He gas atmosphere exhibit high concentration of Pt^{2+}, whereas film deposited under vacuum displays high concentration of Pt^0. Ce reveals mixed Ce^{4+} and Ce^{3+} cations. The grain size of CeO_2 in the $(Pt-CeO_2)$ samples was also influenced by the PLD-background gas pressure. The physical phenomena responsible for such trends are very complex but very interesting from the fundamental point of view and thus deserve further studies.

Among the synthesized samples, the $CNT/Pt-CeO_2$ composite made under 0.5 Torr of helium displayed an unprecedented catalyst activity, high tolerance to CO poisoning judging from chronoamperometric curves, and robust durability towards EOR, compared to pure Pt or to the layer onto layer $CNT/CeO_2/Pt$ architecture. Such remarkable performance of $Pt-CeO_2$ catalyst towards EOR has never been reported to the best of our knowledge. In addition, the free-standing (binderless) catalyst layer structure, the planar deposition of $Pt-CeO_2$ catalyst with its ultra-low loading of Pt (120 μg cm^{-2}) make this anode architecture more appealing for commercial micro DEFCs to power portable electronic systems.

Further significance of this work is that it demonstrates the importance in the design of the catalyst layer architecture principally when it comes to fully benefit from the promoting catalytic properties of CeO_2 in particular. Indeed, we prove here that when CeO_2 material is beneath or when it is mixed with Pt, the interactions between Pt with CeO_2 are not similar leading inevitably to different electrocatalytic performances. Given proper tailoring synthesis conditions, mixed $Pt-CeO_2$ composites are remarkably stable and provide electrochemical performance greater than the layer onto layer CeO_2/Pt architecture. These findings in addition to the planar deposition of $Pt-CeO_2$ catalyst may open new avenue for commercial micro DEFCs to power portable electronic systems.

Appendix A. Supplementary data

Supplementary data related to this article can be found at http://dx.doi.org/10.1016/j.jpowsour.2014.09.114.

References

[1] K. Singh, J. Nowotny, V. Thangadurai, Chem. Soc. Rev. 42 (2013) 1961–1972.
[2] N. Nuraje, R. Asmatulu, S. Kudaibergenov, Curr. Inorg. Chem. 2 (2012) 124–146.
[3] Y. Ren, Z. Ma, P.G. Bruce, Chem. Soc. Rev. 41 (2012) 4909–4927.
[4] F. Vigier, C. Coutanceau, F. Hahn, E.M. Belgsir, C. Lamy, J. Electroanal. Chem. 563 (2004) 81–89.
[5] M.Z.F. Kamarudin, S.K. Kamarudin, M.S. Masdar, W.R.W. Daud, Int. J. Hydrogen Energy 38 (2013) 9438–9453.

[6] S. Carrettin, P. Concepción, A. Corma, J.M. López Nieto, V.F. Puntes, Angew. Chem. Int. Ed. 43 (2004) 2538—2540.
[7] J. Wang, J. Xi, Y. Bai, Y. Shen, J. Sun, L. Chen, W. Zhu, X. Qiu, J. Power Sources 164 (2007) 555—560.
[8] F. Khatkhatay, A. Chen, J.H. Lee, W. Zhang, H. Abdel-Raziq, H. Wang, ACS Appl. Mater. Interfaces 5 (2013) 12541—12547.
[9] O. Parlak, M.M. Demir, ACS Appl. Mater. Interfaces 3 (2011) 4306—4314.
[10] A. Pinna, C. Figus, B. Lasio, M. Piccinini, L. Malfatti, P. Innocenzi, ACS Appl. Mater. Interfaces 4 (2012) 3916—3922.
[11] T. Taniguchi, Y. Sonoda, M. Echikawa, Y. Watanabe, K. Hatakeyama, S. Ida, M. Koinuma, Y. Matsumoto, ACS Appl. Mater. Interfaces 4 (2012) 1010—1015.
[12] A. Younis, D. Chu, I. Mihail, S. Li, ACS Appl. Mater. Interfaces 5 (2013) 9429—9434.
[13] C.T. Campbell, C.H.F. Peden, Science 309 (2005) 713—714.
[14] E. Fabbri, D. Pergolesi, E. Traversa, Chem. Soc. Rev. 39 (2010) 4355—4369.
[15] Z.-P. Li, M. Toshiyuki, G.J. Auchterlonie, J. Zou, D. John, ACS Appl. Mater. Interfaces 3 (2011) 2772—2778.
[16] Y. Chen, Y. Zhang, J. Baker, P. Majumdar, Z. Yang, M. Han, F. Chen, ACS Appl. Mater. Interfaces 6 (2014) 5130—5136.
[17] D.R. Ou, T. Mori, H. Togasaki, M. Takahashi, F. Ye, J. Drennan, Langmuir 27 (2011) 3859—3866.
[18] J. Anderson, A. Karakoti, D.J. Diaz, S. Seal, J. Phys. Chem. C 114 (2010) 4595—4602.
[19] C. Xu, P.K. Shen, Chem. Commun. (2004) 2238—2239.
[20] D. Díaz, N. Greenletch, A. Solanki, A. Karakoti, S. Seal, Catal. Lett. 119 (2007) 319—326.
[21] C. Xu, P.K. Shen, J. Power Sources 142 (2005) 27—29.
[22] Q. He, S. Mukerjee, B. Shyam, D. Ramaker, S. Parres-Esclapez, M.J. Illán-Gómez, A. Bueno-López, J. Power Sources 193 (2009) 408—415.
[23] A. Neto, M. Linardi, D. Anjos, G. Tremiliosi-Filho, E. Spinacé, J. Appl. Electrochem. 39 (2009) 1153—1156.
[24] K. Fugane, T. Mori, D.R. Ou, A. Suzuki, H. Yoshikawa, T. Masuda, K. Uosaki, Y. Yamashita, S. Ueda, K. Kobayashi, N. Okazaki, I. Matolinova, V. Matolin, Electrochim. Acta 56 (2011) 3874—3883.
[25] V. Matolin, I. Matolinova, M. Vaclavu, I. Khalakhan, M. Vorokhta, R. Fiala, I. Pis, Z. Sofer, J. Poltierova-Vejpravova, T. Mori, V. Potin, H. Yoshikawa, S. Ueda, K. Kobayashi, Langmuir 26 (2010) 12824—12831.
[26] H. Tang, H. Sun, D. Chen, X. Jiao, Mater. Lett. 77 (2012) 7—9.
[27] A. Tabet-Aoul, M. Mohamedi, Phys. Chem. Chem. Phys. 14 (2012) 4463—4474.
[28] X. Wang, D. Liu, S. Song, H. Zhang, Chem. Commun. 48 (2012) 10207—10209.
[29] S.K. Meher, G.R. Rao, ACS Catal. 2 (2012) 2795—2809.
[30] S. Sharma, M. Hegde, J. Chem. Phys. 130 (2009) 114706.
[31] P. Bera, A. Gayen, M.S. Hegde, N.P. Lalla, L. Spadaro, F. Frusteri, F. Arena, J. Phys. Chem. B 107 (2003) 6122—6130.
[32] M.A. Scibioh, S.-K. Kim, E.A. Cho, T.-H. Lim, S.-A. Hong, H.Y. Ha, Appl. Catal. B 84 (2008) 773—782.
[33] A. Tselev, A. Gorbunov, W. Pompe, Rev. Sci. Instrum. 72 (2001) 2665—2672.
[34] Z. Hamoudi, M.A.E. Khakani, M. Mohamedi, J. Electrochem. Soc. 159 (2012) B331—B339.
[35] A. Tabet-Aoul, M. Mohamedi, J. Mater. Chem. 22 (2012).
[36] D.B. Chrisey, G.K. Hubler, Pulsed Laser Deposition of Thin Film, John Wiley & Sons, New York, 1994.
[37] A. Pereira, F. Laplante, M. Chaker, D. Guay, Adv. Funct. Mater. 17 (2007) 443—450.
[38] R. Dolbec, E. Irissou, M. Chaker, D. Guay, F. Rosei, M.A. El Khakani, Phys. Rev. B 70 (2004) 201406.
[39] C.D. Wagner, W.M. Riggs, L.E. Davis, J.F. Moulder, Handbook of X-ray Photoelectronic Spectroscopy, Perkin-Elmer Corp, Eden Prairie, MN, 1979.
[40] V. Matolín, M. Cabala, I. Matolínová, M. Škoda, M. Václavů, K.C. Prince, T. Skála, T. Mori, H. Yoshikawa, Y. Yamashita, S. Ueda, K. Kobayashi, Fuel Cells 10 (2010) 139—144.
[41] M. Václavů, I. Matolínová, J. Mysliveček, R. Fiala, V. Matolín, J. Electrochem. Soc. 156 (2009) B938—B942.
[42] P. Bera, K.R. Priolkar, A. Gayen, P.R. Sarode, M.S. Hegde, S. Emura, R. Kumashiro, V. Jayaram, G.N. Subbanna, Chem. Mater. 15 (2003) 2049—2060.
[43] X.L. Tang, B.C. Zhang, Y. Li, Y. Xu, Q. Xin, W.J. Shen, J. Mol. Catal. A Chem. 235 (2005) 122—129.
[44] L. Österlund, S. Kielbassa, C. Werdinius, B. Kasemo, J. Catal. 215 (2003) 94—107.
[45] V. Matolín, M. Cabala, V. Cháb, I. Matolínová, K.C. Prince, M. Škoda, F. Šutara, T. Skála, K. Veltruská, Surf. Interface Anal. 40 (2008) 225—230.
[46] I. Alvarez-Clemares, G. Mata-Osoro, A. Fernández, S. Lopez-Esteban, C. Pecharromán, J. Palomares, R. Torrecillas, J.S. Moya, Adv. Eng. Mater. 12 (2010) 1154—1160.
[47] R. Fiala, I. Khalakhan, I. Matolínová, M. Václavu, M. Vorokhta, Z. Sofer, S. Huber, V. Potin, V. Matolín, J. Nanosci. Nanotechnol. 11 (2011) 5062—5067.
[48] V. Matolín, I. Khalakhan, I. Matolínová, M. Václavů, K. Veltruská, M. Vorokhta, Surf. Interface Anal. 42 (2010) 882—885.
[49] M.S. Dresselhaus, G. Dresselhaus, R. Saito, A. Jorio, Phys. Rep. 409 (2005) 47—99.
[50] J. Spanier, R. Robinson, F. Zhang, S.-W. Chan, I. Herman, Phys. Rev. B 64 (2001) 245407.
[51] W. Weber, K. Hass, J. McBride, Phys. Rev. B 48 (1993) 178—185.
[52] I. Estrela-Lopis, G. Romero, E. Rojas, S. Moya, E. Donath, IOP Publishing, J. Phys. Conf. Ser. (2011) 012017.
[53] Y. Zhang, P.D. Edmondson, T. Varga, S. Moll, F. Namavar, C. Lan, W.J. Weber, Phys. Chem. Chem. Phys. 13 (2011) 11946—11950.
[54] S. Askrabić, R. Kostić, Z. Dohcević-Mitrović, Z.V. Popović, J. Phys. Conf. Ser. 92 (2007) 012042.
[55] S. Maensiri, C. Masingboon, B. Laokul, W. Jareonboon, V. Promarak, P.L. Anderson, S. Seraphin, Cryst. Growth Des. 7 (2007) 950—955.
[56] I. Kosacki, V. Petrovsky, H.U. Anderson, P. Colomban, J. Am. Ceram. Soc. 85 (2002) 2646—2650.
[57] I. Kosacki, T. Suzuki, H.U. Anderson, P. Colomban, Solid State Ionics 149 (2002) 99—105.
[58] J.R. McBride, G.W. Graham, C.R. Peters, W.H. Weber, J. Appl. Phys. 69 (1991) 1596—1604.
[59] W. Lin, A.A. Herzing, C.J. Kiely, I.E. Wachs, J. Phys. Chem. C 112 (2008) 5942—5951.
[60] K. Kinoshita, D.R. Ferrier, P. Stonehart, Electrochim. Acta 23 (1978) 45—54.
[61] T.J. Schmidt, H.A. Gasteiger, G.D. Stäb, P.M. Urban, D.M. Kolb, R.J. Behm, J. Electrochem. Soc. 145 (1998) 2354—2358.
[62] Q.-S. Chen, F.J. Vidal-Iglesias, J. Solla-Gullon, S.-G. Sun, J.M. Feliu, Chem. Sci. 3 (2012) 136—147.
[63] W. Sheng, H.A. Gasteiger, Y. Shao-Horn, J. Electrochem. Soc. 157 (2010) B1529—B1536.
[64] A. Pozio, M. De Francesco, A. Cemmi, F. Cardellini, L. Giorgi, J. Power Sources 105 (2002) 13—19.
[65] H. Wang, Z. Jusys, R.J. Behm, J. Power Sources 154 (2006) 351—359.
[66] T. Iwasita, E. Pastor, Electrochim. Acta 39 (1994) 531—537.
[67] S. Mukerjee, R.C. Urian, Electrochim. Acta 47 (2002) 3219—3231.
[68] A. Cuesta, ChemPhysChem 12 (2011) 2375—2385.